Smart Hybridization of TiO_2 Nanorods and Fe_3O_4 Nanoparticles with Pristine Graphene Nanosheets: Hierarchically Nanoengineered Ternary Heterostructures for High-Rate Lithium Storage

Long Pan, Xiao-Dong Zhu, Xu-Ming Xie, and Yi-Tao Liu**

Today, the ever-increasing demand for large-size power tools has provoked worldwide competition in developing lithium-ion batteries having higher energy and power densities. In this context, advanced anode materials are being extensively pursued, among which TiO_2 is particularly promising owing to its high safety, excellent cost and environmental performances, and high cycle stability. However, TiO_2 is faced with two detrimental deficiencies, that is, extremely low theoretical capacity and conductivity. Herein, a smart hybridization strategy is proposed for the hierarchical co-assembly of TiO_2 nanorods and Fe_3O_4 nanoparticles on pristine graphene nanosheets, aiming to simultaneously address the capacity and conductivity deficiencies of TiO_2 by coupling it with high-capacity (Fe_3O_4) and high-conductivity (pristine graphene) components. The resulting novel, multifunctional ternary heterostructures effectively integrate the intriguing functionalities of the three building blocks: TiO_2 as the major active material can adequately retain such merits as high safety and cycle stability, Fe_3O_4 as the auxiliary active material can contribute extraordinarily high capacities, and pristine graphene as the conductive dopant can guarantee sufficient percolation pathways. Benefiting from a remarkable synergy, the ternary heterostructures deliver superior reversible capacities and rate capabilities, thus casting new light on developing next-generation, high-performance anode materials.

1. Introduction

Today, the energy and environmental crises originating from the excessive exploitation of fossil fuels have provoked fierce competition worldwide in developing secondary power systems that are clean and renewable. In this context, lithium-ion batteries (LIBs) with higher energy and power densities are in vital demand.[1–3] The current anode material, graphite, therefore cannot meet the requirements of next-generation, high-performance LIBs in view of its low theoretical capacity (372 mA h g^{-1}), as well as low Li^+ intercalation potential that may raise serious safety concerns. As such, researchers are showing tremendous enthusiasms in pursuing alternative anode materials being able to exhibit better electrochemical performances.

Among numerous materials advocated as promising anode candidates, nanostructured TiO_2 in the form of, e.g., nanoparticles, nanorods, nanotubes, and beyond[4–18] is inspiring an explosion of research owing to its unique, fascinating features such as excellent cost and environmental performances, short Li^+ diffusion pathways, and more importantly, high cycle stability derived from its negligible volume variation (<4%) upon cycling. In addition, the relatively high operating voltage (1.6–1.8 V vs Li^+/Li) can effectively avoid undesirable electrolyte decomposition as well as lithium plating, thus rendering nanostructured TiO_2 a highly safe anode material. Despite the merits mentioned above, two detrimental deficiencies inherent to nanostructured TiO_2 inevitably prohibit its practical applications: 1) an extremely low theoretical capacity (≈170 mA h g^{-1}) that even fails to compete with graphite; 2) rather disappointing rate capabilities that result from its low intrinsic conductivity (≈10^{-12} S cm^{-1}).

To address the capacity deficiency, several groups have recently attempted to combine nanostructured TiO_2 with a second metal oxide, e.g., Fe_2O_3, Co_3O_4, SnO_2, or MnO_2,[19–27] all of which boast of their extraordinarily high capacities (800–1200 mA h g^{-1}).[28–30] The resulting binary heterostructures can deliver significantly improved capacities, while retaining most of the merits of nanostructured TiO_2. It is worth noting, however, that these metal oxides are all wide-bandgap semiconductors or even insulators, and the inherently low conductivity translates into poor charge transport kinetics leading to rapid capacity fading. The low conductivity is also unfavorable for dissipating the Joule heat generated on the electrode, thus causing intense worries on the battery

L. Pan, Prof. X.-M. Xie, Dr. Y.-T. Liu
Key Laboratory of Advanced Materials (MOE)
Department of Chemical Engineering
Tsinghua University
Beijing 100084, China
E-mail: xxm-dce@mail.tsinghua.edu.cn;
liu-yt03@mails.tsinghua.edu.cn
Prof. X.-D. Zhu
Academy of Fundamental and Interdisciplinary Sciences
Harbin Institute of Technology
Harbin 150080, China

DOI: 10.1002/adfm.201404348

safety. Down to the nanometer size, these metal oxides have an increased electrical resistance owing to increased grain boundaries, further deteriorating the cyclability.

On the other hand, the conductivity deficiency of nanostructured TiO_2 can be solved, in principle, by introducing a conductive dopant such as reduced graphene oxide (*r*-GO).[31–40] When serving as an underlying substrate on which nanostructured TiO_2 is loaded, *r*-GO is able to provide charge transport pathways from the current collector to the electrode. Unfortunately, the oxidation–reduction process employed to produce *r*-GO is intolerable from the environmental point of view since it consumes large quantities of toxic oxidants and/or reductants. Moreover, the electronic properties of *r*-GO are heavily and irreversibly damaged during this process, making its conductivity (ranging from 0.17–3.05 to 41–99 S cm^{-1})[41] rather insufficient and nonuniform compared to that (≈180 S cm^{-1}) of high-quality, pristine graphene directly exfoliated from natural graphite under sonication.[42–45]

In this sense, pristine graphene is highlighted as a higher efficiency conductive dopant than *r*-GO since it is economically and environmentally more viable owing to its milder production conditions. Besides, highly conductive pristine graphene ensures easier charge transport, and is therefore expected to impose better cycle and rate performances.[46] However, binding nanoparticles to pristine graphene is, technically, a huge challenge. The difficulty lies in the chemical inertness of pristine graphene that, unlike *r*-GO, lacks the reactive oxygen moieties facilitating easy functionalization by in situ hydrothermal syntheses[31–40] or electrostatic interactions.[47] In our previous work, we have successfully decorated pristine graphene with metal or metal oxide nanoparticles by complexation interactions.[48] In that case, however, outside linkers (metal ions and organic ligands) are necessary. Herein, we propose, for the first time, a smart hybridization strategy for the hierarchical co-assembly of dual oxide active materials, i.e., TiO_2 nanorods and Fe_3O_4 nanoparticles, on pristine graphene nanosheets based on van der Waals interactions.[49–53] This strategy is aimed to simultaneously address the capacity and conductivity deficiencies of nanostructured TiO_2 by coupling it with high-capacity (Fe_3O_4) and high-conductivity (pristine graphene) components. In addition, the pristine graphene nanosheets can also play two other vital roles: 1) effectively alleviating the strain associated with repeated lithation/delithation and thus buffering the severe volume expansion (>200%) suffered by Fe_3O_4 owing to their large specific surface area (2630 m^2 g^{-1}), as well as superior flexibility and elasticity;[54] 2) substantially contributing to the ultimate electrochemical performances owing to their high theoretical capacity (twice that of graphite). The TiO_2 nanorods and Fe_3O_4 nanoparticles, in turn, can isolate the pristine graphene nanosheets from restacking, thereby preserving the active surfaces. Benefiting from a remarkable synergy, the resulting novel, multifunctional ternary heterostructures deliver strikingly high reversible capacities and rate capabilities, thus casting new light on the development of advanced anode materials for next-generation, high-performance LIBs.

2. Results and Discussion

2.1. Mechanism for Hierarchical Co-Assembly of TiO_2/Fe_3O_4–PG Ternary Heterostructures

The mechanism for the hierarchical co-assembly of TiO_2 nanorods and Fe_3O_4 nanoparticles on pristine graphene nanosheets is illustrated in **Scheme 1**. Basically, natural graphite is directly exfoliated into pristine graphene nanosheets by sonication in a good solvent, *N*-methyl-2-pyrrolidone (NMP), as reported by us previously.[55] The pristine graphene nanosheets are then transferred to a relatively poor solvent, tetrahydrofuran (THF), in which they have a strong tendency to restack owing to unmatched Hansen solubility parameters.[42–45] Note that the Hansen solubility parameters theory is a semiempirical correlation used to describe the dissolution behavior of a solute in a specific solvent,[56] as shown in Equation (1)

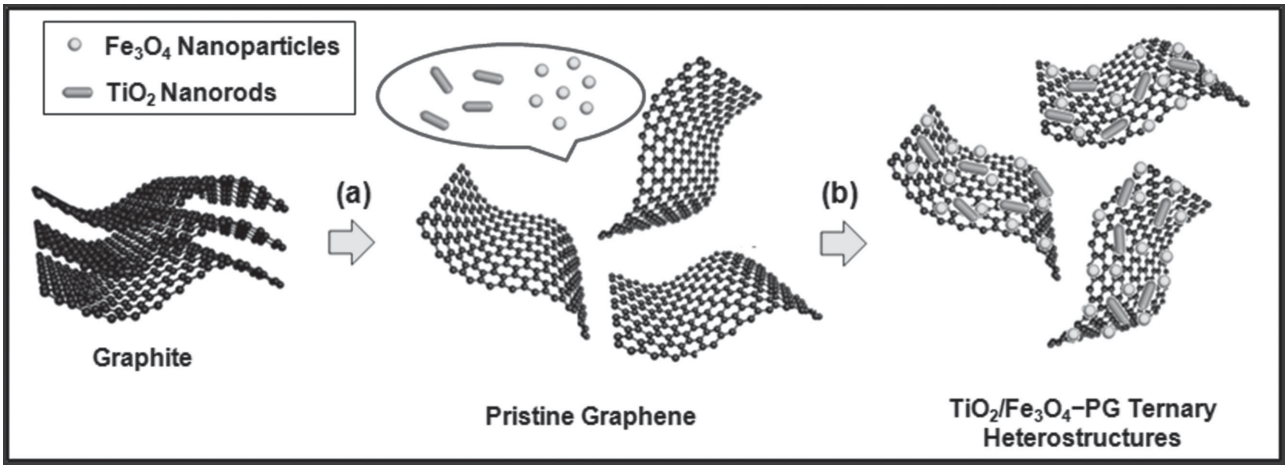

Scheme 1. Mechanism for the hierarchical co-assembly of TiO_2 nanorods and Fe_3O_4 nanoparticles on pristine graphene nanosheets: a) exfoliating natural graphite into pristine graphene nanosheets in NMP by sonication, b) transferring the nanosheets to THF, and introducing TiO_2 nanorods and Fe_3O_4 nanoparticles under magnetic stirring. The organically modified, energetically more stable TiO_2 nanorods and Fe_3O_4 nanoparticles spontaneously and facilely adhere to the naked surfaces of pristine graphene nanosheets through van der Waals interactions, thereby minimizing the total free energy of the solution system and stabilizing the nanosheets in THF by acting as spacers.

$$R_a = \left[4\left(\delta_{D,solv} - \delta_{D,solu}\right)^2 + \left(\delta_{P,solv} - \delta_{P,solu}\right)^2 + \left(\delta_{H,solv} - \delta_{H,solu}\right)^2\right]^{0.5} \quad (1)$$

It takes into consideration such factors as the dispersive (δ_D), polar (δ_P), and hydrogen-bonding (δ_H) solubility parameters of the solute and the solvent. The distance of Hansen solubility parameters, R_a, is a measure of solubility, that is, the smaller the R_a value, the higher the solubility.[57] The Hansen solubility parameters of pristine graphene nanosheets[43] and several representative good and poor solvents,[58] as well as the calculated R_a values, are listed in Table S1 (Supporting Information). As seen from the table, NMP is more effective than THF on solvating the pristine graphene nanosheets owing to its smaller R_a value. It should be stressed that this step is key to the success of the following hierarchical co-assembly, since the huge surface energy of the inadequately solvated pristine graphene nanosheets cannot be compensated for by THF. Therefore, the organically modified, energetically more stable TiO_2 nanorods and Fe_3O_4 nanoparticles, once being introduced, tend to reside on the naked pristine graphene surfaces through van der Waals interactions,[49]–[53] thereby minimizing the total free energy of the solution system and stabilizing the nanosheets in THF by acting as spacers. In a good solvent such as NMP, however, the hierarchical co-assembly is handicapped since the adequately solvated nanosheets have a minimized surface energy, as will be proven below. The present strategy is facile and cost-effective compared to those based on complexation interactions,[48,59] since no specially designed outside linkers are needed. The hierarchically co-assembled ternary heterostructures thus obtained, consisting of TiO_2 nanorods and Fe_3O_4 nanoparticles dually decorated pristine graphene nanosheets, effectively integrate the intriguing functionalities of the three building blocks: the TiO_2 nanorods as the major active material can adequately retain such merits as high cycle stability and structural integrity, the Fe_3O_4 nanoparticles as the auxiliary active material can contribute extraordinarily high capacities, and the pristine graphene nanosheets as the conductive dopant can guarantee sufficient percolation pathways. In addition, the pristine graphene nanosheets can also serve as an underlying substrate to prevent the aggregation of the TiO_2 nanorods and Fe_3O_4 nanoparticles, as well as provide superior flexibility and elasticity to accommodate the strain associated with Li^+ intercalation/deintercalation. The TiO_2 nanorods and Fe_3O_4 nanoparticles, in turn, can serve as spacers to isolate the pristine graphene nanosheets from restacking, thus offering increased gallery spacings for easy Li^+ and charge diffusion. When evaluated as an anode of LIBs, the novel, multifunctional ternary heterostructures display a remarkable synergy on the lithium storage, exhibiting excellent electrochemical performances especially at high rates.

2.2. Characterization of TiO_2/Fe_3O_4–PG Ternary Heterostructures

The detailed characterization of the three building blocks for constructing the ternary heterostructures is presented in **Figure 1** and Figures S1–S10 (Supporting Information). Figure 1a shows a TEM image of a large, thin pristine graphene nanosheet nearly transparent to the electron beam. Note that the flexible and elastic properties of pristine graphene have been well studied, with second- and third-order elastic stiffness as high as 340 and –690 N m^{-1}, respectively, and breaking strength up to 42 N m^{-1}.[54] Ripples characteristic of high flexibility and elasticity can clearly be seen, which, together with the large surface area, are expected to efficiently buffer the severe volume expansion (>200%) suffered by Fe_3O_4 during repeated lithation/delithation.[60] Figure 1b shows an HRTEM image focusing on the white panel in Figure 1a, which reveals a three-layer edge with a gallery spacing of 0.350 nm. The corresponding electron diffraction (ED) pattern in the insert clearly displays a sixfold symmetry of highly crystalline pristine graphene, and the higher (2110) intensity than (1100) is typical of a few-layer graphene nanosheet as proven previously.[42] The quality of our pristine graphene nanosheets is evaluated by Raman spectroscopy, as shown in Figure S2 (Supporting Information). For a carbonaceous material, the intensity ratio of peak D (≈1350 cm^{-1}) to peak G (≈1580 cm^{-1}), I_D/I_G, is often referred to measure its degree of crystallinity.[61] Qualitatively, the I_D/I_G intensity ratio is proportional to the defect concentration. After being exfoliated, the pristine graphene nanosheets have an I_D/I_G value of 0.264, somewhat higher than that (0.082) of natural graphite probably owing to the presence of edge defects. Note that the I_D/I_G value of pristine graphene is much lower than that (>1) of structurally disordered *r*-GO,[62] which may interpret the higher conductivity of the former owing to its better integrity of graphitic network. Both the occurrence of a shoulder designated as peak D′ (≈1600 cm^{-1}) and the shape of peak 2D (≈2700 cm^{-1}, distinct from that of natural graphite) point to the successful production of few-layer graphene.[63,64] The monodisperse, spinel Fe_3O_4 nanoparticles are morphologically examined by TEM, as shown in Figure 1c. The presence of an organic coating layer endows the nanoparticles with excellent solubility in THF without obvious agglomerates. The nanoparticles have a small average diameter of ≈6 nm, which implies a short Li^+ diffusion time and a high Li^+ flux.[65,66] Similarly, a TEM image of organically modified TiO_2 nanorods uniformly dispersed in THF is presented in Figure 1d.

As stated above, when the pristine graphene nanosheets are transferred to a relatively poor solvent, THF, their substantially high surface energy cannot be compensated for.[42–45] Therefore, once the organically modified, energetically more stable TiO_2 nanorods and Fe_3O_4 nanoparticles are introduced, they spontaneously adhere to the naked pristine graphene surfaces through van der Waals interactions, thereby minimizing the total free energy of the solution system and stabilizing the nanosheets in THF by acting as spacers. First, to test the feasibility of this strategy, the Fe_3O_4 nanoparticles and TiO_2 nanorods are employed independently for the hierarchical assembly, and the representative TEM and HRTEM images of the resulting Fe_3O_4–PG or TiO_2–PG binary heterostructures are shown in **Figure 2**. In both cases, the nanoparticles or nanorods are uniformly and densely distributed on the whole nanosheet surfaces with few scattering beyond, emphasizing a fairly high assembling efficiency (Figure 2a,c). It can be seen that even after being densely loaded with these rigid

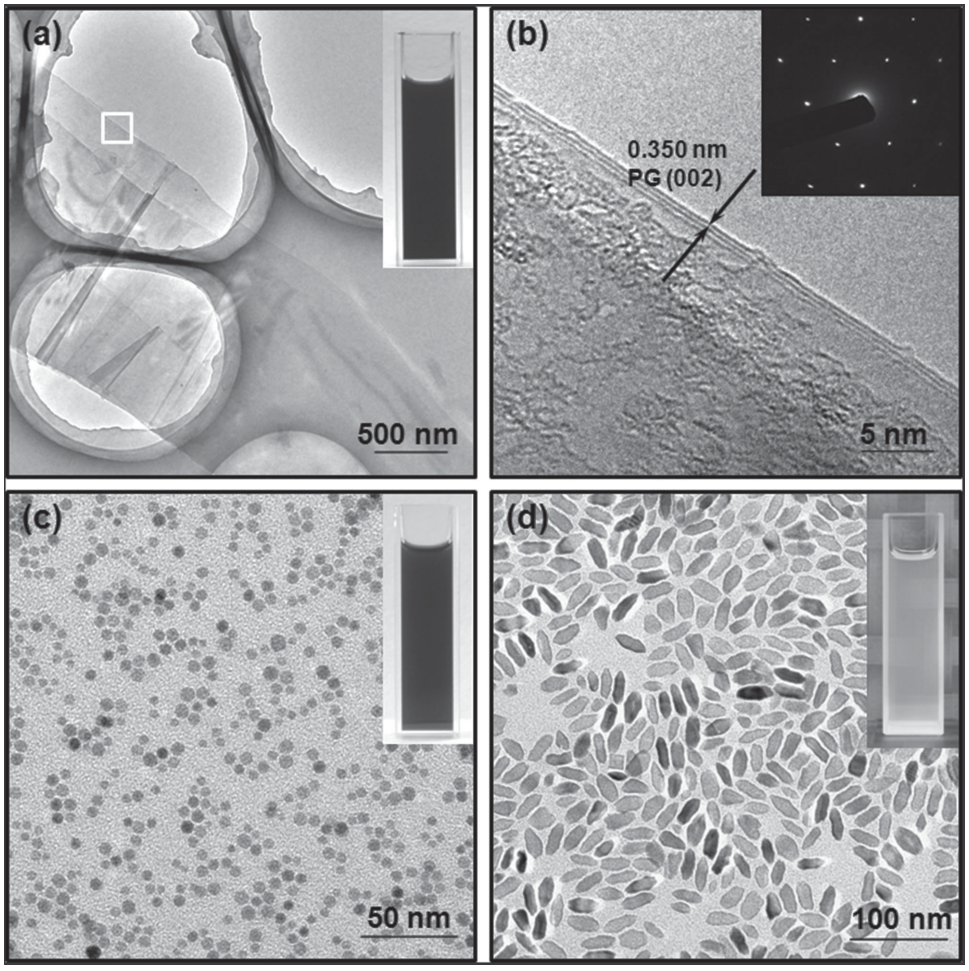

Figure 1. a) TEM image of a large, flexible pristine graphene nanosheet and the corresponding THF solution (inset); b) HRTEM image focusing on the panel in (a) showing a three-layer edge and the corresponding ED pattern (insert); c) TEM image of monodisperse, oleylamine-modified Fe_3O_4 nanoparticles, and the corresponding THF solution (inset); d) TEM image of monodisperse, oleic acid and oleylamine-modified TiO_2 nanorods, and the corresponding THF solution (inset).

nanoparticles or nanorods, the pristine graphene nanosheets are still crumpled. The largely preserved flexibility and elasticity of the nanosheets are applausible for accommodating the strain associated with Li^+ intercalation/deintercalation. Under a closer examination by HRTEM (Figure 2b,d), the lattice fringe spacings of 0.298 and 0.350 nm correspond to the (220) and (101) planes of spinel Fe_3O_4 and anatase TiO_2, respectively, which are in good agreement with the XRD results as shown in Figures S3 and S7 (Supporting Information). Moreover, the (002) plane of pristine graphene can also be discriminated in both the figures. It is worth noting that the affinity between the nanoparticles or nanorods and the nanosheets is high enough to withstand long-time sonication (200 W) without any dissociation.

We stress that the loading density of the nanoparticles or nanorods on the nanosheets can facilely be tuned by varying their feed ratio, as shown in Figures S11 and S12 (Supporting Information). Figure S11 (Supporting Information) displays a series of TEM images of the TiO_2–PG binary heterostructures at different TiO_2/pristine graphene wt ratios. When the fraction of the TiO_2 nanorods is very low (10 wt%), they are only sparsely located on the pristine graphene surfaces. The nanorod loading becomes more compact when the feed ratio is elevated, and a complete, intimate coverage can be found at a TiO_2 fraction of ≈60 wt%. This is also the case for the Fe_3O_4–PG binary heterostructures (Figure S12, Supporting Information). Likewise, a uniform, dense coverage is achieved when the Fe_3O_4 fraction is around 60 wt%, above which excess, unbound nanoparticles can be observed scattering beyond the nanosheets. Furthermore, to demonstrate the importance of the solvent properties in deciding the assembling efficiency, we have conducted a reference experiment in which the pristine graphene nanosheets are dispersed in the mixtures of NMP and THF at various volume ratios. The Fe_3O_4 nanoparticles (60 wt%) are then introduced to these mixed solvents. It is found, interestingly, that the successful assembly is achieved only when the THF fraction is high enough, as shown in Figure S13 (Supporting Information). When the NMP:THF volume ratio is up to 90:10, the nanoparticles are scarcely attached to the pristine graphene surfaces. When the THF fraction is raised to 50 vol%, a moderate loading density of the nanoparticles is witnessed. The loading density is further increased when the

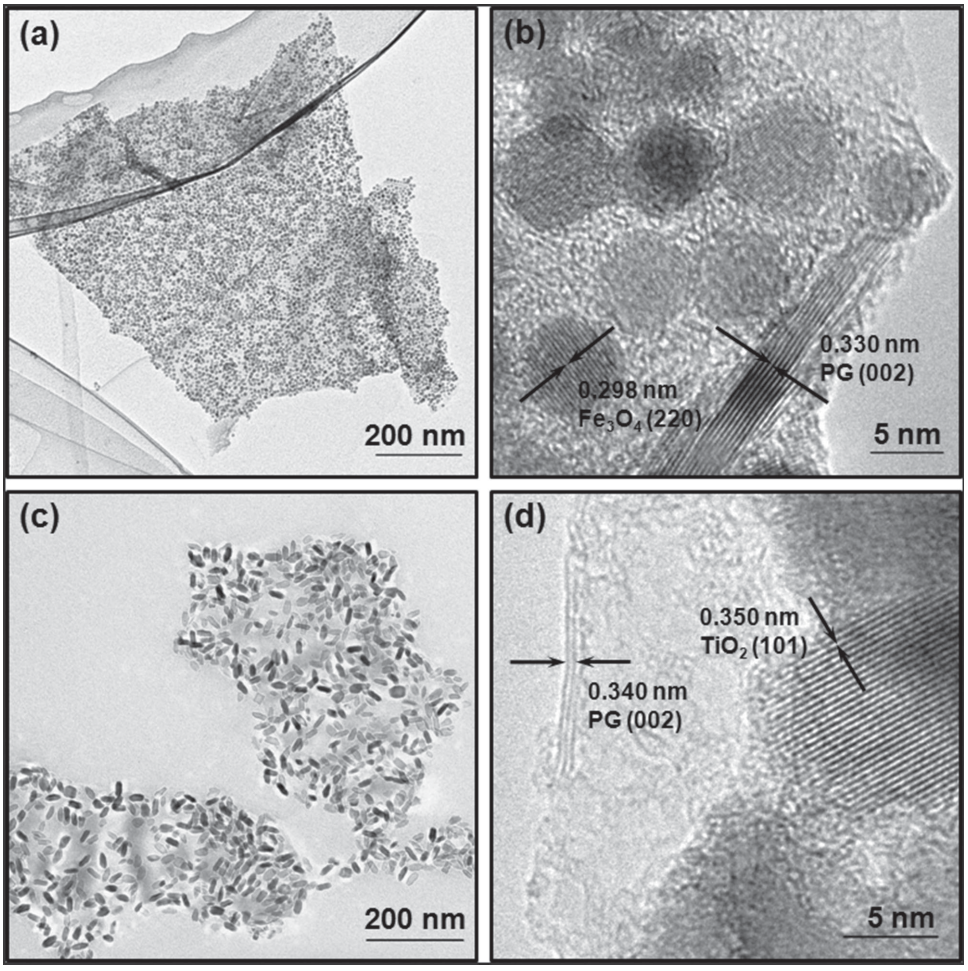

Figure 2. a) TEM and b) HRTEM images of Fe_3O_4–PG binary heterostructures (Fe_3O_4 = 60 wt%, PG = 40 wt%); c) TEM and d) HRTEM images of TiO_2–PG binary heterostructures (TiO_2 = 40 wt%, PG = 60 wt%).

THF fraction is quite high (90 vol%), which is not distinguishable from a THF-only situation as shown in Figure 2a. This phenomenon can be understood from the energy point of view. In other words, the successful assembly is dictated by the competition between the solvent and Fe_3O_4 nanoparticles to reduce the total free energy: Once in an NMP-dominating solvent system, the pristine graphene nanosheets are adequately solvated and thus exist in a relatively stable energy state. Therefore, the Fe_3O_4 nanoparticles can hardly adhere to the pristine graphene surfaces by replacing the NMP molecules since it is not favorable for reducing the surface energy. When the THF fraction is raised, the nanosheets are less solvated owing to unmatched Hansen solubility parameters between the solute and the solvent, and the total free energy of the solution system is increased accordingly. As such, the Fe_3O_4 nanoparticles tend to reside on the pristine graphene surfaces to reduce their otherwise extremely high surface energy. To make clear the effect of other crucial factors, e.g., evaporation rate, on the hierarchical assembly, the NMP:THF (90:10) medium is evaporated at 200 °C before TEM characterization such that NMP is quickly and adequately removed (Figure S14, Supporting Information). As seen from the figure, the attachment of the nanoparticles to the pristine graphene surfaces is neither dense nor uniform. Such a low loading density is very similar to the case shown in Figure S13 (Supporting Information), where the NMP:THF (90:10) medium is evaporated at ambient temperature. Considering this result, we believe that the evaporation rate may not be a crucial factor determining the success or failure of the hierarchical assembly, and the surface properties of pristine graphene in different media may play the most important role.

Starting from these binary heterostructures, we take a big step forward toward novel, multifunctional ternary heterostructures that may integrate the intriguing functionalities of the TiO_2 nanorods, Fe_3O_4 nanoparticles, and pristine graphene nanosheets. **Figure 3**a,b shows representative low- and high-magnification TEM images of the TiO_2/Fe_3O_4–PG ternary heterostructures (40:20:40), respectively. It can be seen that the nanoparticles and nanorods are successfully co-assembled on the pristine graphene nanosheets in a uniform way, and the assembling efficiency is also quite high. Under HRTEM observation (Figure 3c), the (311) and (220) planes of spinel Fe_3O_4 and (101) plane of anatase TiO_2 can easily be identified. Other clues to the coexistence of Fe_3O_4 and TiO_2 on the pristine graphene

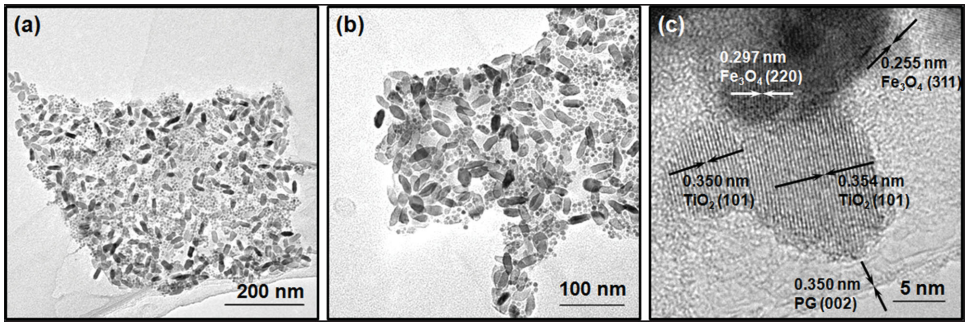

Figure 3. a) Low- and b) high-magnification TEM and c) HRTEM images of TiO_2/Fe_3O_4–PG ternary heterostructures (TiO_2 = 40 wt%, Fe_3O_4 = 20 wt%, PG = 40 wt%).

surfaces are provided by XRD and Raman characterization, as shown in **Figure 4**a,b. As seen from the XRD spectrum of the TiO_2/Fe_3O_4–PG ternary heterostructures, the most prominent peak at 26.55° corresponds to the (002) reflection of few-layer pristine graphene,[67,68] and the calculated gallery spacing of 0.335 nm is in consistent with the value under HRTEM observation (Figure 2b). Besides, diamonds indicating the (220), (311), (511), and (440) reflections of spinel Fe_3O_4 and squares indicating the (101), (004), (200), (204), (220), and (215) reflections of anatase TiO_2 can also be recognized. As to the Raman spectrum, apart from the well-documented, strong peaks (D, G, and 2D) characteristic of pristine graphene, the weak peaks centered at 668 and 144 cm^{-1} are assigned to the A_{1g} mode of spinel Fe_3O_4 and the E_g mode of anatase TiO_2, respectively.[69–71] The I_D/I_G value of pristine graphene in the TiO_2/Fe_3O_4–PG ternary heterostructures is 0.287, verifying that our hierarchical co-assembly based on van der Waals interactions is a noninvasive approach imposing few, if any, new defects on the graphitic network of pristine graphene. The TiO_2/Fe_3O_4–PG ternary heterostructures, after being stably dispersed in THF, can easily be attracted by a magnet owing to the magnetism endowed by the Fe_3O_4 nanoparticles, leaving a nearly transparent solution (Figure S17, Supporting Information). The measured elemental composition of the TiO_2/Fe_3O_4–PG ternary heterostructures (40:20:40) is presented in Table S2 (Supporting Information), which is in consistent with their ratio feed ratio, once again demonstrating the incredibly high assembling efficiency of our strategy.

2.3. Electrochemical Performances of TiO_2/Fe_3O_4–PG Ternary Heterostructures

To elucidate the electrochemical reactions taking place on the TiO_2/Fe_3O_4–PG ternary heterostructures when evaluated as an anode of LIBs, we present the first three cyclic voltammetry (CV) curves (scan rate = 0.1 mV s^{-1}) in **Figure 5**a. As seen from the figure, in the first cathodic scan the reduction peak at 1.53 V originates from Li^+ intercalation according to the following reaction: $TiO_2 + xLi^+ + xe^- \rightarrow Li_xTiO_2$.[72] The strong reduction peak at 0.52 V corresponds to the kinetically activated electrolyte decomposition and the conversion of Fe^{3+} and Fe^{2+} to Fe^0: $Li_xFe_3O_4 + (8-x)Li^+ + (8-x)e^- \rightarrow 3Fe + 4Li_2O$.[73] The reduction peak around 0 V is related to Li^+ intercalation into pristine graphene (Figure S19, Supporting Information), as well as possibly interfacial Li^+ storage.[74] In the second and third cathodic scans, the two reduction peaks at lower potentials become smaller and are almost superposed, indicating that the solid–electrolyte interface (SEI) layer has been built perfectly. The reduction peaks at 0.52 and 1.53 V are positively shifted to 0.69 and 1.70 V owing to the structural modification after the first scan.[74] According to the report of Tarascon et al.,[75] the formation of polymeric species in the alkyl carbonate solution below 2 V results in the growth of a polymeric gel-like layer. These lithium-driven structural and morphological changes are the reasons for the positive shift of the reduction peaks and the increased plateau voltages of the discharging profiles (Figure 5b). In the first anodic scan, the reversible oxidation

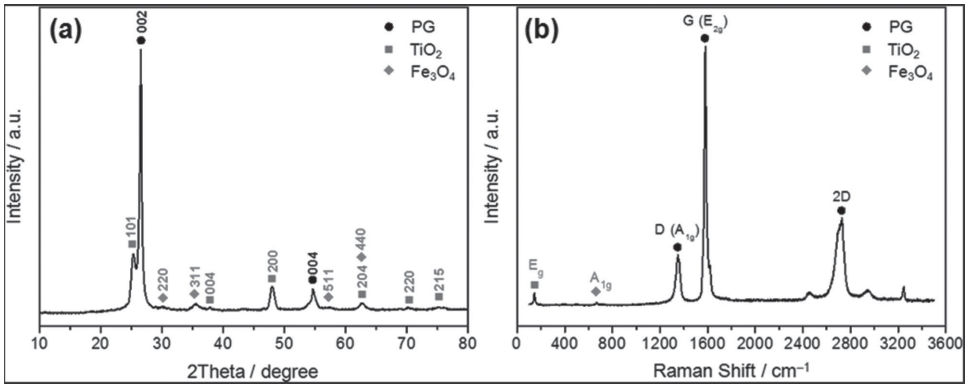

Figure 4. a) XRD and b) Raman spectra of TiO_2/Fe_3O_4–PG ternary heterostructures.

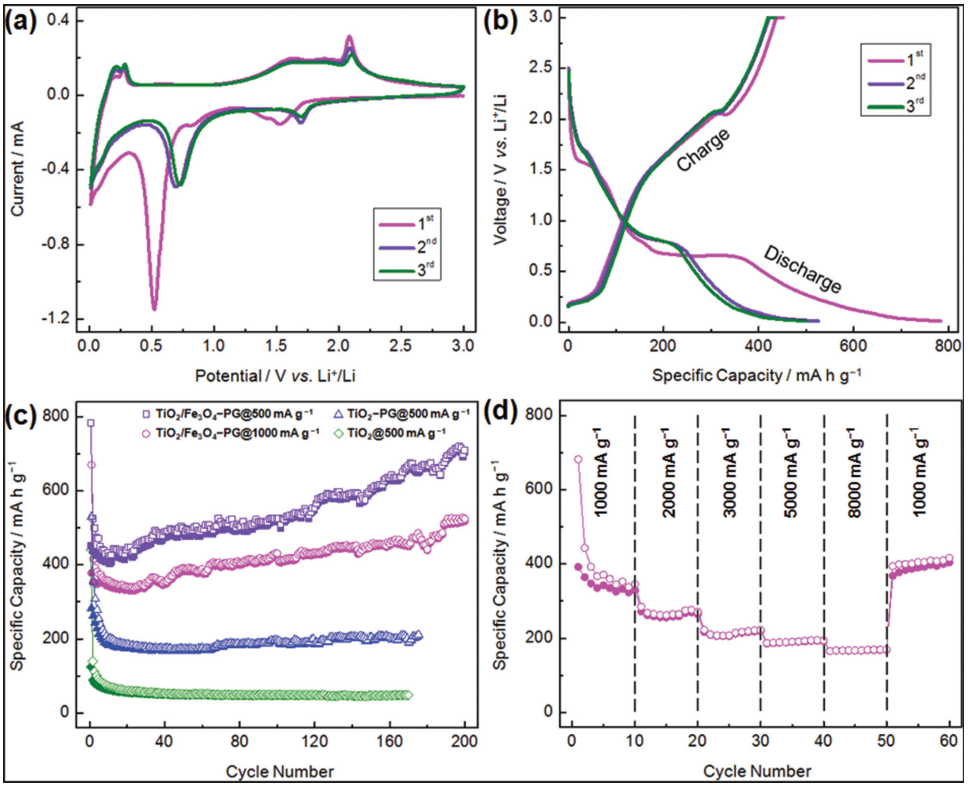

Figure 5. a) CV (scan rate = 0.1 mV s^{-1}) and b) charging–discharging (current density = 500 mA g^{-1}) curves of TiO_2/Fe_3O_4–PG ternary heterostructures; c) cycle behaviors of TiO_2 nanoparticles, TiO_2–PG binary heterostructures, and TiO_2/Fe_3O_4–PG ternary heterostructures at different current densities (500 and 1000 mA g^{-1}); d) rate capabilities of TiO_2/Fe_3O_4–PG ternary heterostructures.

peak at 2.08 V corresponds to the oxidation of Li_xTiO_2 to TiO_2.[22] The broad oxidation peak at 1.60–1.87 V results from the overlapping of two oxidation peaks, which stand for the oxidation of Fe^0 to Fe^{2+} and Fe^{3+}, respectively.[73] Besides, the broad oxidation peak at 0.22–0.29 V is attributed to Li^+ deintercalation from pristine graphene. These oxidation peaks are nearly unchanged from the first to the second cycle, so the potential differences between the cathodic and anodic processes decrease from 1.08–1.35 V to 0.91–1.18 V for the Fe_3O_4/Fe redox couple and from 0.55 V to 0.39 V for the TiO_2/Li_xTiO_2 redox couple. The smaller potential differences of the redox reactions indicate that the TiO_2/Fe_3O_4–PG ternary heterostructures possess higher reversibility from the second cycle (Figure S20, Supporting Information). It is worth noting that from the second scan, both peak current and integrated area intensity are nearly unchanged upon cycling, indicating that there is only a trivial capacity loss during the charging processes. The CV measurements therefore suggest high electrochemical activity and stability of the TiO_2/Fe_3O_4–PG anode.

Figure 5b shows the first three charging–discharging curves of the TiO_2/Fe_3O_4–PG anode at a current density of 500 mA g^{-1}, which are in good agreement with the CV results. The initial discharging and charging capacities are 782 and 451 mA h g^{-1}, respectively. The irreversible capacity loss is ascribed to the electrochemically activated electrolyte decomposition. However, the Coulombic efficiencies soar in the second and third cycles to 83% and 87%. The superior electrochemical performances of the TiO_2/Fe_3O_4–PG anode are further demonstrated by its distinguished cycle behaviors, as shown in Figure 5c. At the end of 200 charging–discharging cycles, a reversible capacity up to 703 mA h g^{-1} is delivered at a current density of 500 mA g^{-1}, corresponding to 90% cycle retention. When the current density is raised to 1000 mA g^{-1}, the TiO_2/Fe_3O_4–PG anode delivers a reversible capacity as high as 524 mA h g^{-1} after 200 cycles, which accounts for 78% cycle retention from the initial capacity. Starting from the ≈20th cycle, the reversible capacities increase steadily, which are generally ascribed to the reversible growth of the polymeric gel-like layer common to transition metal oxides.[76–78] In theory, the reversible growth of the polymeric gel-like layer by the kinetically activated electrolyte decomposition at low potentials is suggested as one of the possible reasons for this phenomenon owing to its ability to coat around the active materials, thus ensuring mechanical cohesion and delivering excess capacities at low potentials through a pseudocapacitive behavior. As to the TiO_2/Fe_3O_4–PG anode, such a behavior therefore results in the stable and gradual capacity increase upon cycling. Tarascon and co-workers[60] thoroughly explored the lithium-driven structural and morphological changes of nanoscale transition metal oxides. Complete disintegration of the starting 100 nm oxide particles into 1–2 nm metal nanoparticles is found when transition metal oxides are fully reduced by lithium. These metal nanoparticles are dispersed in a Li_2O matrix and are surrounded by the SEI layer whose nature and composition vary upon cycling. In our case, the 6 nm Fe_3O_4 nanoparticles are converted to smaller Fe nanoparticles ($Fe_3O_4 + 8Li^+ + 8e^- \rightarrow 3Fe + 4Li_2O$) and thus lose the

crystallinity when fully lithiated. The smaller size and pseudo-amorphous characteristic of the resulting composite electrode translate into an enhanced surface electrochemical reactivity, leading to a steady improvement in the reversible capacities. On the other hand, the formation of Fe nanoparticles during the charging processes enhances the conductivity of the composite electrode. The reduction of the electrode polarization can thus improve the discharging performances step by step. Moreover, Tarascon et al.[75] also found that the in situ formation of highly reactive metallic nanograins at low potentials can promote the growth of a conductive polymeric film. This polymeric gel-like layer can deliver excess capacities at low potentials through a pseudo-capacitive behavior after long-time cycles.[76–78] We think that these factors may be responsible for the stable and steady capacity increase with cycling.

The strikingly high reversible capacities of the TiO_2/Fe_3O_4–PG anode, especially at high rates, compared to those of the TiO_2–*r*-GO anode reported previously, e.g., 190 mA h g^{-1}@320 mA g^{-1},[31] 161 mA h g^{-1}@170 mA g^{-1},[32] 200 mA h g^{-1}@100 mA g^{-1},[33] or 175 mA h g^{-1}@100 mA g^{-1},[34] effectively rationalize our strategy for the smart hybridization of TiO_2 with high-capacity Fe_3O_4 as an auxiliary active material, as well as high-conductivity pristine graphene as a conductive dopant. It is worth mentioning that although several Fe_3O_4-based anodes, e.g., the Fe_3O_4–SWNT (95:5) anode fabricated by Ban et al., deliver a somewhat higher reversible capacity (1000 mA h g^{-1}@930 mA g^{-1}),[79] the TiO_2/Fe_3O_4–PG anode in our work contains only 20 wt% Fe_3O_4 as an auxiliary active material. The major active material is TiO_2, whose unique, fascinating features such as high safety and structural integrity, negligible volume variation, and relatively high operating voltage are well preserved, particularly attractive in practical applications. Moreover, we stress that the cycle retention of the TiO_2/Fe_3O_4–PG anode, being 90% at 500 mA g^{-1} or 78% at 1000 mA g^{-1}, is worth applauding since only a small fraction (20 wt%) of Fe_3O_4 is introduced. As is well known, transition metal oxides other than TiO_2 are notorious for their severe volume expansion during repeated lithation/delithation, leading to awful cycle performances.[60] For example, in the case of a recently developed TiO_2/Fe_2O_3 anode where the Fe_2O_3 fraction is up to 42.9 wt%, the reversible capacity (430.2 mA h g^{-1}@200 mA g^{-1}) after 100 cycles is only ≈61% of the initial value.[80] Such a low cycle retention is also witnessed for other TiO_2-based dual oxide anodes, e.g., TiO_2/Fe_2O_3 (≈68%),[19] TiO_2/MnO_2 (≈60%),[20] or TiO_2/SnO_2 (≈52%).[22]

For comparison, the cycle behaviors of the TiO_2 and TiO_2–PG anodes are also assessed. It is seen that the two controls deliver reversible capacities of only 48 and 212 mA h g^{-1} at 500 mA g^{-1}, corresponding to 11% and 40% cycle retention, respectively. The higher cycle retention of the latter can be attributed to the presence of pristine graphene capable of contributing excellent mechanical properties for stabilizing the SEI layer as well as excellent electronic properties for ensuring sufficient percolation pathways. However, the reversible capacity of the TiO_2–PG anode is much lower than that of the TiO_2/Fe_3O_4–PG anode, once again verifying the importance of introducing a small fraction of Fe_3O_4 that can contribute extraordinarily high capacity. In addition, the TiO_2/Fe_3O_4–PG anode also significantly outperforms the controls in terms of rate capabilities, as shown in Figure 5d. When the current density is 1000, 2000, 3000, or 5000 mA g^{-1}, a reversible capacity of 329, 264, 219, or 192 mA h g^{-1} is delivered. It is encouraging to find that when the current density is further raised to 8000 mA g^{-1}, the reversible capacity is still as high as 169 mA h g^{-1}. When the current density is recovered to 1000 mA g^{-1}, the reversible capacity returns to 404 mA h g^{-1} immediately, revealing a rather high cyclability. To further clarify the effect of pristine graphene on the ultimate electrochemical performances, we have conducted the impedance measurements as shown in Figure S24 (Supporting Information). As seen from the figure, each Nyquist plot is composed of a semicircle in the high-medium frequency region, and a linear tail in the low-frequency region, which are ascribed to the charge transfer and mass transfer of Li^+ ions, respectively.[19] The diameter of the semicircle for the TiO_2/Fe_3O_4–PG ternary heterostructures is much smaller than that of the TiO_2 nanoparticles, verifying the higher conductivity endowed by pristine graphene translating into an excellent cyclability.

3. Conclusion

In conclusion, we have proposed a smart hybridization strategy for the hierarchical co-assembly of TiO_2 nanorods and Fe_3O_4 nanoparticles on pristine graphene nanosheets, aiming to simultaneously address the capacity and conductivity deficiencies of TiO_2 by coupling it with high-capacity (Fe_3O_4) and high-conductivity (pristine graphene) components. The resulting TiO_2/Fe_3O_4–PG ternary heterostructures effectively integrate the intriguing functionalities of the three building blocks, thus achieving a remarkable synergy from the compositional and morphological aspects. Compositionally, the three components can contribute unique properties in a complementary way: (1) the TiO_2 nanorods as the major active material can adequately retain such merits as high cycle stability and safety; (2) the Fe_3O_4 nanoparticles as the auxiliary active material can contribute an extraordinarily high capacity; and (3) the pristine graphene nanosheets as the conductive dopant can guarantee sufficient percolation pathways. Morphologically, the three components constitute novel, multidimensional ternary heterostructures: (1) the pristine graphene nanosheets can serve as an underlying substrate to prevent the aggregation of the TiO_2 nanorods and Fe_3O_4 nanoparticles, as well as provide superior flexibility and elasticity to accommodate the strain associated with Li^+ intercalation/deintercalation; (2) the TiO_2 nanorods and Fe_3O_4 nanoparticles, in turn, can serve as spacers to isolate the pristine graphene nanosheets from restacking, thus offering increased gallery spacings for easy Li^+ and charge diffusion. Benefiting from this remarkable synergy, the TiO_2/Fe_3O_4–PG ternary heterostructures deliver strikingly high reversible capacities and rate capabilities (703 mA h g^{-1}@500 mA g^{-1} and 524 mA h g^{-1}@1000 mA g^{-1}), thus casting new light on the development of advanced anode materials for next-generation, high-performance LIBs.

4. Experimental Section

Raw Materials: Natural graphite powder was purchased from Sinopharm Chemical Reagent Co., Ltd. Iron(III) acetylacetonate

($Fe(acac)_3$) was purchased from Acros Organics BVBA. Oleylamine was purchased from Aladdin Chemical Co., Ltd. Octadecene was purchased from J&K Scientific Ltd. Titanium(IV) butoxide (TB) was purchased from Beijing Xingjin Chemical Works. Absolute alcohol and THF were purchased from Beijing Chemical Works. Oleic acid and NMP were purchased from Xilong Chemical Co., Ltd.

Exfoliation of Pristine Graphene Nanosheets: Natural graphite was added to NMP at an initial concentration of 10 mg mL^{-1}, and then subjected to sonication at 70 W for 48 h. The obtained slurry was centrifuged at 2000 r min^{-1} for 30 min, and the top 1/2 supernatant was collected and vacuum-filtered. The entrapped solid was collected and redispersed in THF by sonication, yielding a dark dispersion as shown in Figure 1a.

Synthesis of Fe_3O_4 Nanoparticles: The synthesis of Fe_3O_4 nanoparticles was adapted from a published paper.[81] Briefly, $Fe(acac)_3$ (3 mmol), oleylamine (30 mL), and octadecene (30 mL) were mixed by magnetic stirring under the protection of nitrogen. The mixture was heated at 280 °C for 1 h, and then cooled naturally to ambient temperature. Absolute alcohol (400 mL) was added, and the synthesized Fe_3O_4 nanoparticles were separated out by a magnet. The product was further washed by absolute alcohol twice, and vacuum-dried at 40 °C overnight. Note that the obtained Fe_3O_4 nanoparticles could readily be dispersed in THF, yielding a brown dispersion as shown in Figure 1c.

Synthesis of TiO_2 Nanorods: The synthesis of TiO_2 nanorods was performed according to a previous report.[82] Typically, TB (5 mmol), oleylamine (25 mmol), oleic acid (25 mmol), and absolute ethanol (100 mmol) were mixed in a 35 mL Teflon cup and stirred for 10 min. The Teflon cup was then placed in a 130 mL Teflon-lined stainless-steel autoclave containing 20 mL ethanol solution (96 vol%). The system was heated to 180 °C and kept at that temperature for 18 h. The obtained TiO_2 nanorods were washed by absolute alcohol twice and vacuum-dried at 40 °C overnight. Note that the obtained TiO_2 nanorods could readily be dispersed in THF, yielding a milky white dispersion as shown in Figure 1d.

Hierarchical Co-Assembly of TiO_2/Fe_3O_4–PG Ternary Heterostructures: In a typical experiment, TiO_2 nanorods, Fe_3O_4 nanoparticles, and pristine graphene nanosheets were mixed in THF at various wt ratios, and the mixtures were left under magnetic stirring for a couple of hours. During the stirring process, the organically modified TiO_2 nanorods and Fe_3O_4 nanoparticles spontaneously adhered to the naked surfaces of the pristine graphene nanosheets. The obtained TiO_2/Fe_3O_4–PG ternary heterostructures were collected by vacuum filtration, rinsed by THF three times, and vacuum-dried at 40 °C overnight. Individual Fe_3O_4 nanoparticles or TiO_2 nanorods were also assembled on the pristine graphene nanosheets in the same way for comparison.

Electrochemical Tests: An anode was prepared by coating a copper foil (current collector) with a slurry containing 70 wt% active material, 20 wt% acetylene black, and 10 wt% poly(vinylidene fluoride) dissolved in NMP. The anode was then dried in vacuum at 120 °C for 12 h to adequately evaporate the residual organic solvent, and equipped in a half cell according to the configuration of (–) Li | electrolyte | anode (+) with a liquid electrolyte (1 M solution of $LiPF_6$ in ethylene carbonate/dimethyl carbonate at a volume ratio of 1:1) in a vacuum glove box. A microporous polypropylene membrane was used as the separator.

Characterization: TEM was performed by a Hitachi HT7700 microscope operated at an accelerating voltage of 100 kV. HRTEM was performed by a JEOL JEM-2010 microscope operated at an accelerating voltage of 120 kV. SPM was performed on a Shimadzu SPM-9700 microscope in the tapping mode. FTIR spectra were recorded by a Nicolet 560 spectrometer. XPS spectra were recorded by an Escalab 250 Xi. XRD patterns were recorded by a Bruker D8 Advanced X-ray diffractometer with Cu Kα radiation (λ = 0.154 nm). Raman spectra were recorded by a LabRAM HR Evolution spectrometer (λ = 514 nm). TGA curves were obtained by a Shimadzu DTG-60 analyzer in N_2 at a heating rate of 10 °C min^{-1}. The BET measurement was performed by a Quantachrome Autosorb-1 Canalyzer (USA). The elemental composition was determined by a Varian VISTA-MTX inductively coupled plasma mass spectrometry (ICP–MS).

Supporting Information

Supporting Information is available from the Wiley Online Library or from the author.

Acknowledgements

L.P. and X.-D.Z. contributed equally to this work. The authors sincerely thank the financial support from the National Natural Science Foundation of China (Nos. 21304053 and 21274079) and the Specialized Research Fund for the Doctoral Program of Higher Education (No. 20120002130012). Y.-T.L. is grateful to the China Postdoctoral Science Foundation (No. 2014T70077). X.-D.Z. is grateful to the Natural Science Foundation of Heilongjiang (No. B201202) and the Postdoctoral Science–Research Development Foundation of Heilongjiang (No. LBH-Q11130).

Received: December 9, 2014
Revised: April 2, 2015
Published online: April 20, 2015

[1] K. Xie, B. Wei, *Adv. Mater.* **2014**, *26*, 3592.
[2] B. Scrosati, J. Hassoun, Y.-K. *Sun, Energy Environ. Sci.* **2011**, *4*, 3287.
[3] H. Guan, X. Wang, H. Li, C. Zhi, T. Zhai, Y. Bando, D. Golberg, *Chem. Commun.* **2012**, *48*, 4878.
[4] Y. Tang, Y. Zhang, J. Deng, J. Wei, H. L. Tam, B. K. Chandran, Z. Dong, Z. Chen, X. Chen, *Adv. Mater.* **2014**, *26*, 6111.
[5] S. Liu, Z. Wang, C. Yu, H. B. Wu, G. Wang, Q. Dong, J. Qiu, A. Eychmüller, X. W. Lou, *Adv. Mater.* **2013**, *25*, 3462.
[6] T. Xia, W. Zhang, J. B. Murowchick, G. Liu, X. Chen, *Adv. Energy Mater.* **2013**, *3*, 1516.
[7] D. Pan, H. Huang, X. Wang, L. Wang, H. Liao, Z. Li, M. Wu, *J. Mater. Chem. A* **2014**, *2*, 11454.
[8] N. D. Petkovich, S. G. Rudisill, B. E. Wilson, A. Mukherjee, A. Stein, *Inorg. Chem.* **2014**, *53*, 1100.
[9] X. Li, Y. Chen, L. Zhou, Y.-W. Mai, H. Huang, *J. Mater. Chem. A* **2014**, *2*, 3875.
[10] J. Liu, W. Liu, K. Chen, S. Ji, Y. Zhou, Y. Wan, D. Xue, P. Hodgson, Y. Li, *Chem. Eur. J.* **2013**, *19*, 9811.
[11] B. Oschmann, D. Bresser, M. N. Tahir, K. Fischer, W. Tremel, S. Passerini, R. Zentel, *Macromol. Rapid Commun.* **2013**, *34*, 1693.
[12] W. Wang, Q. Sa, J. Chen, Y. Wang, H. Jung, Y. Yin, *ACS Appl. Mater. Interfaces* **2013**, *5*, 6478.
[13] X. Wang, Y. Yan, B. Hao, G. Chen, *ACS Appl. Mater. Interfaces* **2013**, *5*, 3631.
[14] T. Song, H. Han, H. Choi, J. W. Lee, H. Park, S. Lee, W. I. Park, S. Kim, L. Liu, U. Paik, *Nano Res.* **2014**, *7*, 491.
[15] Z. Wang, X. W. Lou, *Adv. Mater.* **2012**, *24*, 4124.
[16] J. S. Chen, Y. L. Tan, C. M. Li, Y. L. Cheah, D. Y. Luan, S. Madhavi, F. Y. C. Boey, L. A. Archer, X. W. Lou, *J. Am. Chem. Soc.* **2010**, *132*, 6124.
[17] J. S. Chen, L. A. Archer, X. W. Lou, *J. Mater. Chem.* **2011**, *21*, 9912.
[18] H. B. Wu, J. S. Chen, X. W. Lou, H. H. Hng, *Nanoscale* **2011**, *3*, 4082.
[19] J. Luo, X. Xia, Y. Luo, C. Guan, J. Liu, X. Qi, C. F. Ng, T. Yu, H. Zhang, H. J. Fan, *Adv. Energy Mater.* **2013**, *3*, 737.
[20] J.-Y. Liao, D. Higgins, G. Lui, V. Chabot, X. Xiao, Z. Chen, *Nano Lett.* **2013**, *13*, 5467.
[21] Y. Luo, J. Luo, J. Jiang, W. Zhou, H. Yang, X. Qi, H. Zhang, H. J. Fan, D. Y. W. Yu, C. M. Li, T. Yu, *Energy Environ. Sci.* **2012**, *5*, 6559.
[22] J.-H. Jeun, K.-Y. Park, D.-H. Kim, W.-S. Kim, H.-C. Kim, B.-S. Lee, H. Kim, W.-R. Yu, K. Kang, S.-H. Hong, *Nanoscale* **2013**, *5*, 8480.

[23] L. Yu, Z. Wang, L. Zhang, H. B. Wu, X. W. Lou, *J. Mater. Chem. A* **2013**, *1*, 122.
[24] X. Hou, X. Wang, B. Liu, Q. Wang, Z. Wang, D. Chen, G. Shen, *Chem. Electro Chem.* **2014**, *1*, 108.
[25] Z. Yang, Q. Meng, Z. Guo, X. Yu, T. Guo, R. Zeng, *J. Mater. Chem. A* **2013**, *1*, 10395.
[26] Z. Yang, G. Du, Z. Guo, X. Yu, Z. Chen, T. Guo, R. Zeng, *Nanoscale* **2011**, *3*, 4440.
[27] Y.-M. Lin, R. K. Nagarale, K. C. Klavetter, A. Heller, C. B. Mullins, *J. Mater. Chem.* **2012**, *22*, 11134.
[28] Z. Wang, L. Zhou, X. W. Lou, *Adv. Mater.* **2012**, *24*, 1903.
[29] J. Jiang, Y. Li, J. Liu, X. Huang, C. Yuan, X. W. Lou, *Adv. Mater.* **2012**, *24*, 5166.
[30] H. B. Wu, J. S. Chen, H. H. Hng, X. W. Lou, *Nanoscale* **2012**, *4*, 2526.
[31] R. Mo, Z. Lei, K. Sun, D. Rooney, *Adv. Mater.* **2014**, *26*, 2084.
[32] S. Ding, J. S. Chen, D. Luan, F. Y. C. Boey, S. Madhavi, X. W. Lou, *Chem. Commun.* **2011**, *47*, 5780.
[33] B. Qiu, M. Xing, J. Zhang, *J. Am. Chem. Soc.* **2014**, *136*, 5852.
[34] W. Li, F. Wang, S. Feng, J. Wang, Z. Sun, B. Li, Y. Li, J. Yang, A. A. Elzatahry, Y. Xia, D. Zhao, *J. Am. Chem. Soc.* **2013**, *135*, 18300.
[35] S. Yang, X. Feng, K. Müllen, *Adv. Mater.* **2011**, *23*, 3575.
[36] X. Xin, X. Zhou, J. Wu, X. Yao, Z. Liu, *ACS Nano* **2012**, *6*, 11035.
[37] X. Jiang, X. Yang, Y. Zhu, H. Jiang, Y. Yao, P. Zhao, C. Li, *J. Mater. Chem. A* **2014**, *2*, 11124.
[38] T. Hu, X. Sun, H. Sun, M. Yu, F. Lu, C. Liu, J. Lian, *Carbon* **2013**, *51*, 322.
[39] Y. Luo, J. Luo, W. Zhou, X. Qi, H. Zhang, D. Y. W. Yu, C. M. Li, H. J. Fan, T. Yu, *J. Mater. Chem. A* **2013**, *1*, 273.
[40] J. S. Chen, Z. Wang, X. C. Dong, P. Chen, X. W. Lou, *Nanoscale* **2011**, *3*, 2158.
[41] Z.-Q. Duan, Y.-C. Sun, Y.-T. Liu, X.-M. Xie, X.-D. Zhu, *RSC Adv.* **2014**, *4*, 41543.
[42] Y. Hernandez, V. Nicolosi, M. Lotya, F. M. Blighe, Z. Sun, S. De, I. T. McGovern, B. Holland, M. Byrne, Y. K. Gun'ko, J. J. Boland, P. Niraj, G. Duesber, S. Krishnamurthy, R. Goodhue, J. Hutchison, V. Scardaci, A. C. Ferrari, J. N. Coleman, *Nat. Nanotechnol.* **2008**, *3*, 563.
[43] Y. Hernandez, M. Lotya, D. Rickard, S. D. Bergin, J. N. Coleman, *Langmuir* **2009**, *26*, 3208.
[44] U. Khan, A. O'Neill, M. Lotya, S. De, J. N. Coleman, *Small* **2010**, *6*, 864.
[45] J. N. Coleman, *Adv. Funct. Mater.* **2009**, *19*, 3680.
[46] X. Cao, Y. Shi, W. Shi, X. Rui, Q. Yan, J. Kong, H. Zhang, *Small* **2013**, *9*, 3433.
[47] L.-L. Li, K.-P. Liu, G.-H. Yang, C.-M. Wang, J.-R. Zhang, J.-J. Zhu, *Adv. Funct. Mater.* **2011**, *21*, 869.
[48] Y.-T. Liu, Z.-Q. Duan, X.-M. Xie, X.-Y. Ye, *Chem. Commun.* **2013**, *49*, 1642.
[49] L. Pan, X.-D. Zhu, X.-M. Xie, Y.-T. Liu, *J. Mater. Chem. A* **2015**, *3*, 2726.
[50] L. Pan, K.-X. Wang, X.-D. Zhu, X.-M. Xie, Y.-T. Liu, *J. Mater. Chem. A* **2015**, *3*, 6477.
[51] G. A. Rance, D. H. Marsh, S. J. Bourne, T. J. Reade, A. N. Khlobystov, *ACS Nano* **2010**, *4*, 4920.
[52] M. Ding, Y. Tang, A. Star, *J. Phys. Chem. Lett.* **2013**, *4*, 147.
[53] X. Wang, G. Meng, C. Zhu, Z. Huang, Y. Qian, K. Sun, X. Zhu, *Adv. Funct. Mater.* **2013**, *23*, 5771.
[54] C. Lee, X. Wei, J. W. Kysar, J. Hone, *Science* **2008**, *321*, 385.
[55] Y.-T. Liu, X.-M. Xie, X.-Y. Ye, *Carbon* **2011**, *49*, 3529.
[56] C. M. Hansen, *Hansen Solubility Parameters: A User's Handbook*, CRC, Boca Raton, FL **2007**.
[57] K.-G. Zhou, N.-N. Mao, H.-X. Wang, Y. Peng, H.-L. Zhang, *Angew. Chem. Int. Ed.* **2011**, *50*, 10839.
[58] J. N. Coleman, *Acc. Chem. Res.* **2013**, *46*, 14.
[59] L. Pan, Y.-T. Liu, X.-M. Xie, X.-D. Zhu, *Chem. Asian J.* **2014**, *9*, 1519.
[60] P. Poizot, S. Laruelle, S. Grugeon, L. Dupont, J. M. Tarascon, *Nature* **2000**, *407*, 496.
[61] M. S. Dresselhaus, A. Jorio, M. Hofmann, G. Dresselhaus, R. Saito, *Nano Lett.* **2010**, *10*, 751.
[62] Y.-T. Liu, X.-D. Zhu, Z.-Q. Duan, X.-M. Xie, *Chem. Commun.* **2013**, *49*, 10305.
[63] A. C. Ferrari, J. C. Meyer, V. Scardaci, C. Casiraghi, M. Lazzeri, F. Mauri, S. Piscanec, D. Jiang, K. S. Novoselov, S. Roth, A. K. Geim, *Phys. Rev. Lett.* **2006**, *97*, 187401.
[64] L. Guardia, M. J. Fernández-Merino, J. I. Paredes, P. Solís-Fernández, S. Villar-Rodil, A. Martínez-Alonso, J. M. D. Tascón, *Carbon* **2011**, *49*, 1653.
[65] Y. Chen, B. Song, L. Lu, J. Xue, *Nanoscale* **2013**, *5*, 6797.
[66] Y. Chen, B. Song, M. Li, L. Lu, J. Xue, *Adv. Funct. Mater.* **2014**, *24*, 319.
[67] A. Malesevic, R. Vitchev, K. Schouteden, A. Volodin, L. Zhang, G. Van Tendeloo, A. Vanhulsel, C. Van Haesendonck, *Nanotechnology* **2008**, *19*, 305604.
[68] N. Liu, F. Luo, H. Wu, Y. Liu, C. Zhang, J. Chen, *Adv. Funct. Mater.* **2008**, *18*, 1518.
[69] X. Sun, C. Zheng, F. Zhang, Y. Yang, G. Wu, A. Yu, N. Guan, *J. Phys. Chem. C* **2009**, *113*, 16002.
[70] T. Ohsaka, F. Izumi, Y. Fujiki, *J. Raman Spectrosc.* **1978**, *7*, 321.
[71] W. F. Zhang, Y. L. He, M. S. Zhang, Z. Yin, Q. Chen, *J. Phys. D: Appl. Phys.* **2000**, *33*, 912.
[72] C. Zhu, X. Xia, J. Liu, Z. Fan, D. Chao, H. Zhang, H. J. Fan, *Nano Energy* **2014**, *4*, 105.
[73] C. He, S. Wu, N. Zhao, C. Shi, E. Liu, J. Li, *ACS Nano* **2013**, *7*, 4459.
[74] T. Yoon, C. Chae, Y.-K. Sun, X. Zhao, H. H. Kung, J. K. Lee, *J. Mater. Chem.* **2011**, *21*, 17325.
[75] S. Laruelle, S. Grugeon, P. Poizot, M. Dollé, L. Dupont, J.-M. Tarascon, *J. Electrochem. Soc.* **2002**, *149*, A627.
[76] W. Wei, S. Yang, H. Zhou, I. Lieberwirth, X. Feng, K. Müllen, *Adv. Mater.* **2013**, *25*, 2909.
[77] J. Luo, J. Liu, Z. Zeng, C. F. Ng, L. Ma, H. Zhang, J. Lin, Z. Shen, H. J. Fan, *Nano Lett.* **2013**, *13*, 6136.
[78] Y. Chen, B. Song, X. Tang, L. Lu, J. Xue, *Small* **2014**, *10*, 1536.
[79] C. Ban, Z. Wu, D. T. Gillaspie, L. Chen, Y. Yan, J. L. Blackburn, A. C. Dillon, *Adv. Mater.* **2010**, *22*, E145.
[80] L. Gao, H. Hu, G. Li, Q. Zhu, Y. Yu, *Nanoscale* **2014**, *6*, 6463.
[81] J. Xie, C. Xu, Z. Xu, Y. Hou, K. L. Young, S. X. Wang, N. Pourmand, S. Sun, *Chem. Mater.* **2006**, *18*, 5401.
[82] C.-T. Dinh, T.-D. Nguyen, F. Kleitz, T.-O. Do, *ACS Nano* **2009**, *3*, 3737.